Simulation-based study of wind–wave interactions under various sea conditions

HAO Xuan-ting, LI Tian-yi, CAO Tao, SHEN Lian

(Department of Mechanical Engineering and Saint Anthony Falls Laboratory,
University of Minnesota, Minneapolis, Minnesota 55455, USA, Email: shen@umn.edu)

Abstract：Despite their impact on the ocean environment, key physical processes in wind-wave interactions are poorly understood. Using a solver developed for undulatory boundaries, we perform numerical simulations of wind-wave systems under various sea conditions, including wind over monochromatic waves, early wind-wave generation, and wind over a broadband wave field. Our results show that the wave direction and wave age can significantly change the streamwise vorticity distribution in the wind field. Different wave patterns are observed in the process of wind-wave generation. In a broadband wave field, the wave growth rate due to wind input is found to depend on the wave steepness.

Key words：wind-wave interaction, direct numerical simulation, large eddy simulation, phase-resolved wave simulation

1 Introduction

Connecting the marine atmospheric boundary layer and the upper ocean, wind-wave interactions play a critical role in the ocean environment. While there have been extensive studies on the physical processes in wind-wave interactions[1], the fundamental mechanisms remain elusive due to the complexity in wind and wave fields. On the ocean, the wind is highly turbulent, and the wave field is nonlinear and irregular. On the other hand, a better understanding of these processes can help improve the performance of large-scale climate models[2]. In recent years, numerical simulations have been widely used in the study of wind-wave interactions with the advancement in computing power[3-5]. In particular, numerical simulations based on the Navier–Stokes equations have proven to be an accurate and valuable approach to investigate the fundamental mechanism of the interaction between wind and waves.

In the present study, we perform high-fidelity simulations to explore the physical processes in wind-wave interactions. We aim to improve the understanding on these physical processes by examining the role of key physical parameters such as wind speed, peak wave length, and wave steepness. In the following sections, we first review the numerical method we use[6-8] and problem setup, and then present the simulation results under different sea conditions.

2 Numerical Method and Problem Setup

In the present study, the wind simulation is based on a solver developed for simulation of viscous flows with undulatory boundaries[6-8]. We briefly review the basic solver. The Navier–Stokes equations are first transformed from the physical domain to the computational domain through the following coordinate transformation: $\tau = t$, $\xi = x$, $\psi = y$, $\zeta = (z-\eta)/(\bar{H}-\eta)$, where $\eta = \eta(x,y,t)$ is the ocean surface elevation and $\bar{H}$ is the mean vertical height of the physical domain. The transformed equations are:

$$\frac{\partial u}{\partial \xi} + \zeta_x \frac{\partial u}{\partial \zeta} + \frac{\partial v}{\partial \psi} + \zeta_y \frac{\partial v}{\partial \zeta} + \zeta_z \frac{\partial w}{\partial \zeta} = 0 \tag{1}$$

$$\begin{aligned} &\frac{\partial u}{\partial \tau} + \zeta_t \frac{\partial u}{\partial \zeta} + u\left(\frac{\partial u}{\partial \xi} + \zeta_x \frac{\partial u}{\partial \zeta}\right) + v\left(\frac{\partial u}{\partial \psi} + \zeta_y \frac{\partial u}{\partial \zeta}\right) + w\zeta_z \frac{\partial u}{\partial \zeta} \\ &= -\frac{1}{\rho_a}\left(\frac{\partial p^*}{\partial \xi} + \zeta_x \frac{\partial p^*}{\partial \zeta}\right) + \nu_a \nabla^2 u \end{aligned} \tag{2}$$

$$\begin{aligned} &\frac{\partial v}{\partial \tau} + \zeta_t \frac{\partial v}{\partial \zeta} + u\left(\frac{\partial v}{\partial \xi} + \zeta_x \frac{\partial v}{\partial \zeta}\right) + v\left(\frac{\partial v}{\partial \psi} + \zeta_y \frac{\partial v}{\partial \zeta}\right) + w\zeta_z \frac{\partial v}{\partial \zeta} \\ &= -\frac{1}{\rho_a}\left(\frac{\partial p^*}{\partial \psi} + \zeta_y \frac{\partial p^*}{\partial \zeta}\right) + \nu_a \nabla^2 v \end{aligned} \tag{3}$$

$$\frac{\partial w}{\partial \tau} + \zeta_t \frac{\partial w}{\partial \zeta} + u\left(\frac{\partial w}{\partial \xi} + \zeta_x \frac{\partial w}{\partial \zeta}\right) + v\left(\frac{\partial w}{\partial \psi} + \zeta_y \frac{\partial w}{\partial \zeta}\right) + w\zeta_z \frac{\partial w}{\partial \zeta}$$

$$=-\frac{1}{\rho_a}\left(\zeta_z\frac{\partial p^*}{\partial \zeta}\right)+\nu_a\nabla^2 w \tag{4}$$

Here, (u, v, w) denote wind velocities, ρ_a is the air density, ν_a is the air viscosity, and p^* is the modified pressure.

The time derivative then becomes:

$$\frac{\partial}{\partial t}=\frac{\partial}{\partial \tau}+\frac{\zeta-1}{\bar{H}-\tilde{\eta}}\frac{\partial \tilde{\eta}}{\partial t} \tag{5}$$

In the computational domain, the Laplace operator is:

$$\nabla^2=\frac{\partial^2}{\partial \xi^2}+\frac{\partial^2}{\partial \psi^2}+2\zeta_x\frac{\partial^2}{\partial \xi \partial \zeta}+2\zeta_y\frac{\partial^2}{\partial \psi \partial \zeta}+(\zeta_x^2+\zeta_y^2+\zeta_z^2)\frac{\partial^2}{\partial \zeta^2}+(\zeta_{xx}+\zeta_{yy})\frac{\partial}{\partial \zeta} \tag{6}$$

While the solver was originally developed for direct numerical simulation (DNS), it can be easily extended to large eddy simulation (LES) to accommodate the needs of simulating the coupled wind-wave system under various sea conditions. In the present study, we consider three types of canonical problems, namely monochromatic waves, developing wave field from an initially flat surface, and a broadband wave field. For the first type of problems, the wind turbulence is resolved using wall-resolved LES. The wave motions are prescribed using the Airy wave solution, which provides the necessary Dirichlet boundary condition of the surface velocity and geometry to the wind turbulence solver. For the second type, our focus is on the early stage of wind-wave growth, and a DNS solver similar to that for wind simulation is used to simulate the wave field. On the water side, Neumann boundary condition of velocity, i.e., the shear stress, and Dirichlet boundary condition of pressure are imposed on the top of the domain. The continuity of interface velocity and shear stress is achieved through an effective iteration scheme. Fully nonlinear kinematic and dynamic boundary conditions on the wave surface are enforced. In the third case, the wind turbulence is simulated using wall-modelled LES, and the wave motions are resolved using a high-order spectral (HOS) model[9]. More details of the numerical scheme and validations can be found in literature[6-8].

The simulation parameters are summarized in Table 1. The wave ages in the monochromatic wave cases WFW01, WOW01, WOW04, and broadband wave case BRDW are defined as c_p/U_0, where c_p denotes the peak wave speed and U_0 denotes the mean wind speed at the top of the physical domain. Similarly, the Reynolds numbers in these cases are defined as

$U_0\lambda_p/\nu$, with λ_p denoting the peak wave length. In the case CWW, because the focus is on the transient process of the early-stage wave growth, the properties of the characteristic wave component, such as the peak wave, change too rapidly during the simulation to define a characteristic wave age value cannot be defined. The Reynolds numbers in this case are defined as $u_*^a\bar{H}^a/\nu^a$ and $u_*^w\bar{H}^w/\nu^w$, where the superscripts a and w denotes the air side and the water side, respectively. In all cases, the wind turbulence is initialized with random fluctuations added to a mean profile and first simulated with no-slip boundary condition over a flat surface. When fully developed, the wind turbulence is coupled with different wave solvers. For case BRDW, the initial wave field is constructed from an empirical spectrum[10] and each individual wave component is assigned a random phase. For case CWW, the data is collected immediately at the time of wind-wave coupling, while for others, the data is not collected until a sufficiently long time for the wind-wave field to fully develop.

Table 1 Summary of simulation parameters

Cases	Numerical Scheme	Grid Resolution	Wave age	Reynolds Number
WFW01	Wall-resolved LES (wind) – prescribed airy wave	$(384,384,193)$	0.1	30000
WOW01			−0.1	
WOW04			−0.4	
CWW	DNS (wind) – DNS (wave)	$(128,128,128)$ (wind) $(128,128,128)$ (wave)	Changing with time	268 (air side) 120 (water side)
BRDW	Wall-modelled LES (wind) – HOS (wave)	$(256,128,256)$ (wind) $(512,256)$ (wave)	0.54	4.8×10^6

3 Results

In the first part of study, we investigate the turbulence statistics in a three-dimensional top-velocity-driven Couette flow over progressive water waves (Fig. 1). To examine the effects of the propagating direction and speed of surface wave on the wind field, we adopt three different wave ages (Table 1). Here, the positive wave age means that the surface wave is travelling following the mean wind, while the negative wave age represents the opposite case. The Airy wave solution is used to prescribe the motions of the progressive water waves.

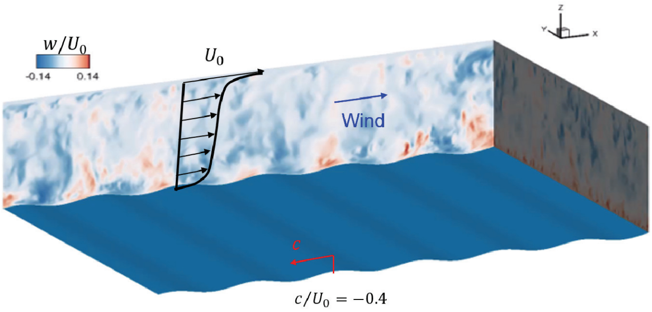

Fig. 1 Instantaneous field of vertical velocity in the wind opposing wave case WOW04.

Fig. 2 illustrates the phase-averaged field of $z^+ \overline{\omega_x\omega_x}^+$ in case WFW01, WOW01, and WOW04. As shown, both the propagating direction and speed of the surface wave remarkably affect the intensity of $z^+ \overline{\omega_x\omega_x}^+$. Specifically, by comparing results between case WFW01 and WOW01, one can clearly observe that under the opposing wave condition, the intensity of $z^+ \overline{\omega_x\omega_x}^+$ is much smaller than that in the following wave case. Moreover, as the opposing wave speed increases, the suppression of $z^+ \overline{\omega_x\omega_x}^+$ is more pronounced, as illustrate by Fig. 4(c). In addition to the intensity, the location of strong streamwise vorticity varies with both progressive direction and speed of the surface wave. As illustrated by Fig. 2(a) and (b), our results show that the area of high $z^+ \overline{\omega_x\omega_x}^+$ shifts closer to the surface wave crest in the opposing wave case, and this trend is more obvious as the opposing surface wave propagates faster.

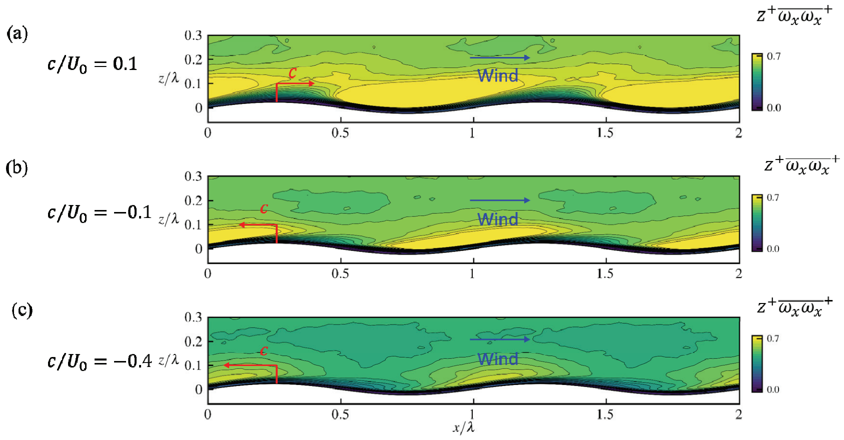

Fig. 2 Contours of phase-averaged $z^+\overline{\omega_x\omega_x}^+$ in the turbulent wind field over surface gravity waves of various wave ages (see Table 1): (a) WFW01, (b) WOW01, and (c) WOW04. The superscript '+' denotes normalization by wall units.

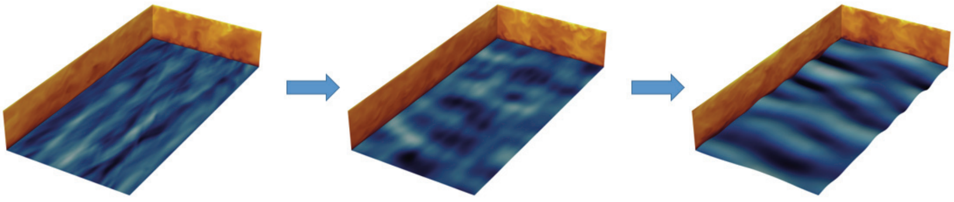

$tU_0^a/H^a = 10$ $tU_0^a/H^a = 500$ $tU_0^a/H^a = 1000$

Fig. 3 Different patterns of wave field during the wind-wave generation process.

In the case CWW, the simulation domains are $(L_x, L_y, H^a) = (2\pi, \pi, 1)$ and $(L_x, L_y, H^w) = (2\pi, \pi, 1)$ for the air side and water side, respectively. The density ratio and viscosity ratio between air and water are kept realistic. The non-dimensional time step based on the top air velocity U_0^a and domain height H^a is chosen as $tU_0^a H^a = 0.001$. When the wind is exerted, the turbulent airflow distorts the flat water surface and irregular wave patterns grow with the time. Fig. 3 shows different times of the wind-wave generation process. The surface patterns see a drastic change from the initial streak-like pattern to the eventually wave-dominant pattern. Fig. 4 shows an instantaneous flow field when the dominant wave patterns have been generated.

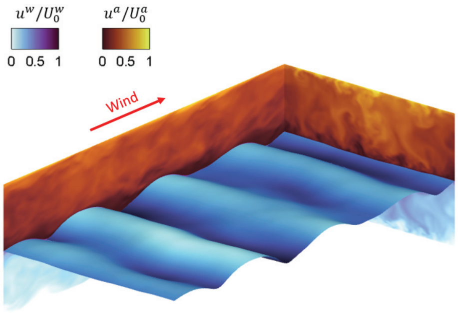

Fig. 4 Instantaneous flow field when dominant waves have been generated by turbulent wind.

In the final part, we examine a wind-wave system of realistic parameters, with wind turbulence simulated over a broadband wave field. To illustrate the effect of broad-band waves on the momentum transfer, we calculate the quadrant ratio $Q_r = -(Q2+Q4)/(Q1+Q3)$ as a function of the wage age c_p/U_a following Sullivan *et al.*[11] Here $Qi\ (i=1,2,3,4)$ denotes the turbulent momentum flux in different quadrants[12] and U_a is a reference speed in the wind field. As shown in Fig. 3, the quadrant ratio in the present study is close to the values found in previous experiments and simulations[2,11,13-15], indicating that the contribution of ejections and sweeps dominates the momentum flux.

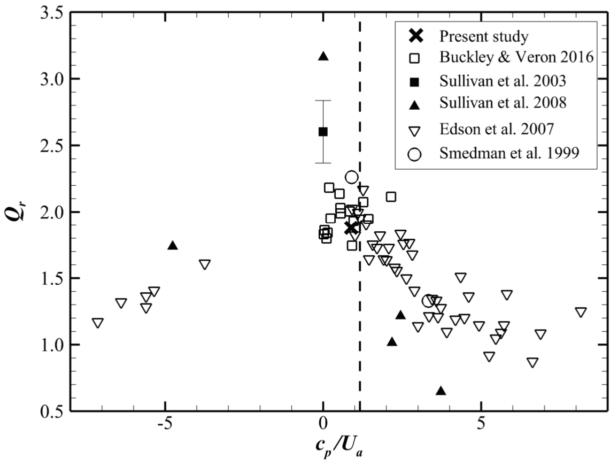

Fig. 3 Quadrant ratio as a function of the wave age. The vertical dashed line denotes the boundary of wind-wave equilibrium.

The wave growth rate due to the work done by the pressure in the wind field is defined by[16-17]:

$$\beta = \frac{2}{\lambda (ak)^2}\int_0^{\lambda} \frac{p}{\rho_a u_*^2}\frac{\partial \eta}{\partial x}\mathrm{d}x$$

Compared with monochromatic waves, the broadband wave field contains multiple wave components and the above equation cannot be used directly to calculate β. To address this issue, we use a technique developed by Liu *et al.*[18] to estimate β based on Fourier decomposition. In Fig. 4, we plot β as a function of the wave steepness ak. In the present study, the maximum wave steepness of the broadband wave field is around 0.10. The wave components are not as steep as the monochromatic waves and narrow-band waves in previous studies[4,19-24]. Therefore, the values of β are much lower than the upper limit when the stress at the air-water surface is entirely balanced by the form drag. Our result is reasonably well compared with the compiled data from literature. It should be noted that Fig. 4 cannot be used directly for determining the quantitative relation between the wave growth rate and wave steepness, because wave age can also affect its value.

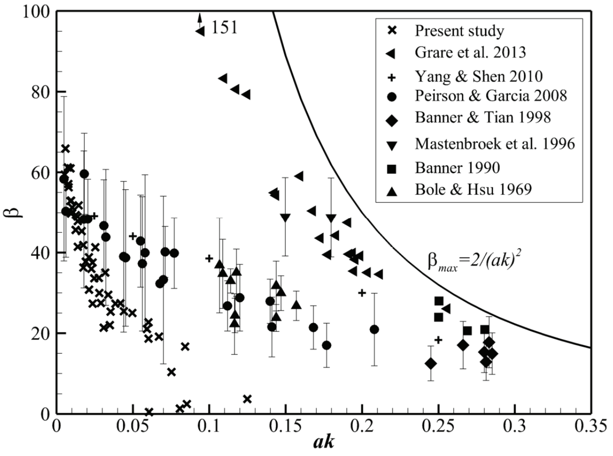

Fig. 4 Wave growth rate as a function of wave steepness. The black solid line denotes the theoretical upper limit.

4 Conclusions

We have performed numerical simulations of the coupled wind-wave system under different sea conditions. The wind turbulence solvers include DNS, wall-modeled LES, and wall-resolved LES. The wave motions are prescribed in wind over monochromatic wave cases, and resolved using the DNS solver and HOS method in the wind-wave generation case and the broadband wave case, respectively. In the monochromatic wave cases, the wave directions and wave ages are found to have a controlling impact on the streamwise vorticity in wind turbulence. In the process of wind-wave generation, the wave field changes from a streak-dominant pattern to a wave-dominant pattern. The result of the broadband wave case, where wind and waves are close to equilibrium, shows that the wave energy growth induced by wind input is dependent on the wave steepness.

References

1 Sullivan PP, McWilliams JC. 2010. Dynamics of winds and currents coupled to surface waves. Annu. Rev. Fluid Mech. 42:19–42

2 Edson J, Crawford T, Crescenti J, Farrar T, Frew N, et al. 2007. The coupled boundary layers and air-sea transfer experiment in low winds. Bull. Am. Meteorol. Soc. 88(3):341–356

3 Sullivan PP, Mcwilliams JC, Moeng C. 2000. Simulation of turbulent flow over idealized water waves. J. Fluid Mech. 404:47–85

4 Yang D, Shen L. 2010. Direct-simulation-based study of turbulent flow over various waving boundaries. J. Fluid Mech. 650:131–180

5 Zonta F, Soldati A, Onorato M. 2015. Growth and spectra of gravity--capillary waves in countercurrent air/water turbulent flow. J. Fluid Mech. 777:245–259

6 Yang D, Shen L. 2011. Simulation of viscous flows with undulatory boundaries. Part I: Basic solver. J. Comput. Phys. 230(14):5488–5509

7 Yang D, Shen L. 2011. Simulation of viscous flows with undulatory boundaries: Part II. Coupling with other solvers for two-fluid computations. J. Comput. Phys. 230(14):5510–5531

8 Yang D, Meneveau C, Shen L. 2013. Dynamic modelling of sea-surface roughness for large-eddy simulation of wind over ocean wavefield. J. Fluid Mech. 726:62–99

9 Dommermuth DG, Yue DKP. 1987. A high-order spectral method for the study of nonlinear gravity waves. J. Fluid Mech. 184:267–288

10 Hasselmann K, Barnett TP, Bouws E, Carlson H, Cartwright DE, et al. 1973. Measurements of Wind-Wave

Growth and Swell Decay during the Joint North Sea Wave Project (JONSWAP). Deutsches Hydrographisches Institut

11 Sullivan PP, Edson JB, Hristov T, McWilliams JC. 2008. Large-eddy simulations and observations of atmospheric marine boundary layers above nonequilibrium surface waves. J. Atmos. Sci. 65(4):1225–1245

12 Wallace JM, Eckelmann H, Brodkey RS. 1972. The wall region in turbulent shear flow. J. Fluid Mech. 54(01):39

13 Smedman A, Högström U, Bergström H, Rutgersson A. 1999. A case study of air--sea interaction during swell conditions. J. Geophys. Res. Ocean. 104:25833–25851

14 Sullivan PP, Horst TW, Lenschow DH, Moeng C-H, Weil JC. 2003. Structure of subfilter-scale fluxes in the atmospheric surface layer with application to large-eddy simulation modelling. J. Fluid Mech. 482:101–139

15 Buckley MP, Veron F. 2016. Structure of the airflow above surface waves. J. Phys. Oceanogr. 46(5):1377–1397

16 Donelan MA. 1999. Wind-induced growth and attenuation of laboratory waves. In Wind-over-Wave Couplings: Perspectives and Prospects, eds. SG Sajjadi, NH Thomas, JCR Hunt, pp. 183–94. Clarendon

17 Li PY, Xu D, Taylor PA. 2000. Numerical modelling of turbulent airflow over water waves. Boundary-Layer Meteorol. 95(3):397–425

18 Liu Y, Yang D, Guo X, Shen L. 2010. Numerical study of pressure forcing of wind on dynamically evolving water waves. Phys. Fluids. 22(4):041704

19 Bole JB, Hsu EY. 1969. Response of gravity water waves to wind excitation. J. Fluid Mech. 35(04):657–675

20 Banner ML. 1990. The influence of wave breaking on the surface pressure distribution in wind-wave interactions. J. Fluid Mech. 211:463–495

21 Mastenbroek C, Makin VK, Garat MH, Giovanangeli JP. 1996. Experimental evidence of the rapid distortion of turbulence in the air flow over water waves. J. Fluid Mech. 318:273–302

22 Banner ML, Tian X. 1998. On the determination of the onset of breaking for modulating surface gravity water waves. J. Fluid Mech. 367:107–137

23 Peirson WL, Garcia AW. 2008. On the wind-induced growth of slow water waves of finite steepness. J. Fluid Mech. 608:243–274

24 Grare L, Peirson WL, Branger H, Walker JW, Giovanangeli J-P, Makin V. 2013. Growth and dissipation of wind-forced, deep-water waves. J. Fluid Mech. 722:5–50